

Simultaneous Observation of Nonlinear Magneto-Optical Rotation in the Temporal and Spectral Domains with an Electro-Optic Frequency Comb

Nathanial Wilson,^{1,*} Nicolas Bourbeau Hébert,^{1,2} Christopher Perrella,¹ Philip Light,¹ Jérôme Genest,^{1,2} Szymon Pustelný,³ and André Luiten¹

¹*Institute for Photonics and Advanced Sensing (IPAS), and School of Physical Sciences, The University of Adelaide, South Australia 5005, Australia*

²*Centre d'Optique, Photonique et Laser, Université Laval, Québec, QC G1V 0A6, Canada*

³*Marian Smoluchowski Institute of Physics, Jagiellonian University, Łojasiewicza 11, Kraków 30-348, Poland*



(Received 25 March 2018; published 7 September 2018)

We simultaneously observe the Larmor precession of rubidium atoms in both the temporal and spectral domains using an electro-optically generated frequency comb. Rubidium vapor is optically pumped on the $F = 2 \rightarrow F' = 1$ hyperfine transition of the ^{87}Rb D₁ manifold, while its response is observed with a frequency comb that spans 8 GHz of the spectrum with a temporal resolution of 9.78 μs . The frequency comb modes experience optical rotation by interacting with the $F = 2 \rightarrow F' = 1, 2$ transitions. The spectral and temporal resolution of the comb allows us to observe that there are two separate channels for polarized atoms to appear in the probe beam: one pathway where atoms travel directly from the pump to the probe region, and a secondary pathway that involves interaction of the polarized atoms with the cell walls. The unique features of the comb allow a direct estimate of the relative density of polarized atoms in the vapor cell, as well as a measurement of the quality of the antirelaxation coating on the cell walls. We show that rotation measurements with the comb approach the limits set by photon shot noise.

DOI: 10.1103/PhysRevApplied.10.034012

I. INTRODUCTION

The ability to measure magnetic fields with high sensitivity is important for a myriad of applications, including medical diagnoses and imaging [1–5], measurements of geomagnetism [6], and fundamental physics research [7–10]. One approach to highly sensitive magnetometry exploits nonlinear magneto-optical effects in which a polarized medium undergoes temporal evolution due to interactions with external electromagnetic fields. This temporal evolution results in measurable modulation of the optical parameters of light transmitted through the medium [11]. Through the use of antirelaxation coatings, ultranarrow magneto-optical resonances on the order of approximately 1 Hz can be observed [12], which enables ultrasensitive magnetometry to be performed.

Nonlinear magneto-optical effects are conventionally observed using a continuous-wave (CW) probe laser, which naturally interacts with the medium at just a single optical frequency. This observation frequency is usually chosen to be at the center of a Doppler-broadened transition in order to obtain the highest interaction strength

[13]. However, in this paper we use an electro-optic frequency comb (EOFC) [14–21] as the probe, which allows real-time observations at multiple optical frequencies. This alternative approach has the capability of exploring physical processes such as collisional transfer of higher-order polarization moments between alkali atoms [22], as well as the processes that lead to polarization of the atomic population.

The comb is generated using an electro-optic modulator and enables spectroscopy with temporal and spectral resolutions that approach the limits set by the Fourier transform [16,17]. The ability to simultaneously resolve both temporal and spectral domains provides deep insight into physical processes and can allow observation of previously unobserved effects such as the role of radiation reabsorption in nonlinear spectroscopy [17].

Here, the unique features of the comb are used to show that there are multiple pathways to produce polarized atoms in the medium, that these pathways have different temporal evolutions, and that the fraction of pumped atoms within the vapor cell is approximately 4.4%. Furthermore, a comparison is made between the noise of optical rotation measurements made with a frequency comb and the noise that arises in the conventional approach of a continuous-wave laser. We show that both techniques are compatible with photon shot-noise-limited performance.

*nathanial.wilson@adelaide.edu.au

II. EXPERIMENTAL SETUP

The experimental setup is shown in Fig. 1. The magneto-optical effects are generated in a 50-mm-long rubidium vapor cell that has a paraffin coating on the cell walls to extend the spin-relaxation time to approximately 100 μ s. The vapor density is set to approximately 7×10^{10} atoms/cm³ [23] by heating the cell to 315 K (42 °C), where the temperature is accurately measured using the Doppler width of the optical transitions [24]. The cell is housed within a three-layer cylindrical μ -metal magnetic shield with a measured shielding factor of approximately 1800 to provide a quiet magnetic environment. Within the innermost shield, a constant-bias magnetic field of approximately 0.8 μ T is generated along the longitudinal axis using a Helmholtz coil.

Both pump and probe light propagate through the rubidium vapor parallel to the magnetic field in a conventional Faraday geometry [13], with a beam displacement of approximately 10 mm. The pump beam originates from an external cavity diode laser (ECDL), which is stabilized to a frequency that is 175 MHz red-detuned from the ⁸⁷Rb $F = 2 \rightarrow F' = 1$ hyperfine transition using saturated absorption spectroscopy. The pump is amplitude modulated via an acousto-optic modulator (AOM) to produce either a single pulse for the free-induction decay (FID) measurements or a continuous train of pulses for the synchronously pumped measurements. The pump beam has a $1/e^2$ diameter of 1.5 mm with a peak power of 15 mW input to the cell and is linearly polarized along the vertical using a Glan-Thompson (GT) prism.

The atomic vapor is probed with an EOFC, which is generated by passing 795-nm radiation from a titanium-sapphire laser through a high-bandwidth, high-index electro-optic modulator (EOM). The EOM is driven between two phase states in accordance with a pseudorandom binary sequence (PRBS). The modulation generates an optical spectrum consisting of a comb of sidebands with a frequency separation of 39.37 MHz, set by the repetition rate of the PRBS. The comb has an approximate sinc² power envelope with its first zeros ± 5 GHz away from the seed laser's frequency. The generation of the EOFC, as well as its temporal and spectral profile, is presented in further detail in Ref. [16].

At the input to the vapor cell, the comb is linearly polarized at 45° from vertical by a GT prism. A total comb power of 500 μ W reaches the cell, corresponding to approximately 4 μ W per mode near the center of the comb. Analysis of the comb's polarization rotation through the vapor cell is achieved using a vertically aligned Wollaston prism (WP), which separates the two orthogonal polarization components. Each of these components is then coupled into single-mode optical fibers.

In parallel, a fraction of the titanium-sapphire light is frequency shifted by an AOM to generate a local oscillator

(LO) signal. This LO is then combined with the two outputs of the Wollaston prism, and the resulting mixing products are detected by separate high-bandwidth photodetectors. The photodetector signals are simultaneously recorded on two channels of a high-speed oscilloscope (2.5-GHz bandwidth, with a sample rate of 20 GS/s).

A total of 500 μ s of data is recorded in order to observe the temporal evolution of the rubidium spectrum. The data is sliced into 9.78- μ s-long segments by integrating 385 consecutive binary sequences. Each segment is individually Fourier transformed, producing time-resolved spectra with both a high temporal ($\Delta t = 9.78 \mu$ s) and spectral ($\Delta\nu = 39.37$ MHz) resolution. To improve the signal-to-noise ratio, the data presented here consist of 400 averages. The spectral shape of the comb is measured using a reference path (cf. Fig. 1) that bypasses the vapor cell, enabling calibration of the optical and electrical transfer functions.

The transmission $T_{\text{exp}}(\omega, t)$ and optical rotation $\phi_{\text{exp}}(\omega, t)$ experienced by each mode of the EOFC can be calculated using the powers measured on the two photodetectors P_1 and P_2 , together with the total incident comb power P_0 , via

$$T_{\text{exp}}(\omega, t) = \frac{P_1 + P_2}{P_0}, \quad (1)$$

$$\phi_{\text{exp}}(\omega, t) = \frac{1}{2} \arcsin \left(\frac{P_1 - P_2}{P_1 + P_2} \right), \quad (2)$$

where the incident power is measured using the reference path. Figure 2 displays the measured rubidium transmission spectrum $T_{\text{exp}}(\omega)$, along with a nonlinear fit of the

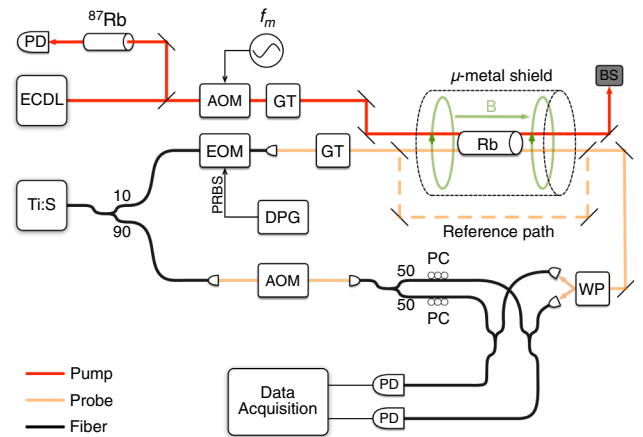


FIG. 1. Simplified experimental setup, showing the external cavity diode laser (ECDL), titanium-sapphire laser (Ti:S), acousto-optic modulator (AOM), Glan-Thompson prism (GT), Wollaston prism (WP), photodetector (PD), beam stopper (BS), polarization controller (PC), electro-optic modulator (EOM), and digital pattern generator (DPG).

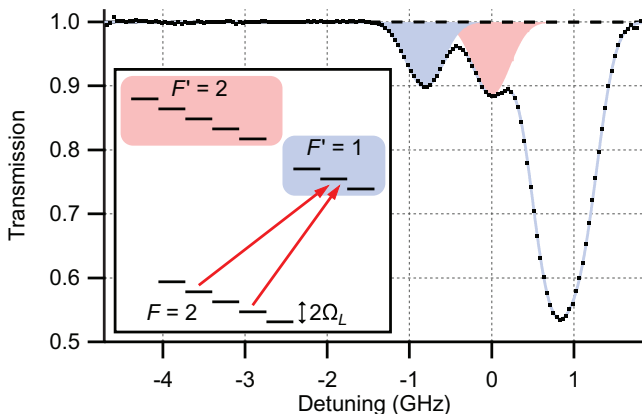


FIG. 2. Rubidium D₁ spectrum as measured by the EOFC with an integration time of $400 \times 9.78 \mu\text{s}$ (dots), with a fit using Eq. (3). The inset shows the Zeeman sublevels of ⁸⁷Rb involved in the nonlinear magneto-optical effects observed with the comb, with one possible transition that is connected by the probe radiation shown using red arrows. The shaded features in the transmission spectrum correspond to the optical transitions between the levels shown in the inset, while the unshaded features are associated with the ⁸⁵Rb isotope ($F = 3 \rightarrow F' = 2, 3$).

form

$$T_{\text{fit}}(\omega) = \exp \left(- \sum_i \alpha_i \exp \left[\frac{(\omega - \omega_i)^2}{2\sigma^2} \right] \right), \quad (3)$$

where the sum is performed over all hyperfine transitions. Here, σ is the Doppler width, while α_i and ω_i are the optical depth and frequency detuning of the i th allowed transition, respectively.

III. THEORETICAL ANALYSIS

The observation of the atomic vapor with a frequency comb provides insight into the production and relaxation of optically polarized atoms. This section of the paper aims to provide a clear theoretical framework for discussion of the experimental observations.

We measure the temporally and spectrally dependent polarization changes that are imposed on the probe beam in order to track the response of the medium to both optical pumping and the influence of an external magnetic field. The optical rotation of the transmitted probe, $\phi_{\text{th}}(\omega, t)$, is calculated by decomposing the incident optical probe into right- and left-circularly polarized components (σ_+ and σ_- , respectively) and determining the influence on each of these by their associated complex refractive indices, $\eta_+(\omega, t)$ and $\eta_-(\omega, t)$ [25]:

$$\phi_{\text{th}}(\omega, t) = \frac{\omega l}{2c} \text{Re} [\eta_+(\omega, t) - \eta_-(\omega, t)], \quad (4)$$

while the optical depth of the probe, under the condition that $\text{Im}[\eta_+(\omega, t)] = \text{Im}[\eta_-(\omega, t)]$ (valid for symmetric

ground-state distributions), is given by [26]

$$\alpha_{\text{th}}(\omega, t) = \frac{2\omega l}{c} \text{Im} [\eta_{\pm}(\omega, t)], \quad (5)$$

where l is the sample length, ω is the angular frequency of the probe radiation, and c is the speed of light.

Within an atomic vapor at thermal equilibrium, the population distribution over the Zeeman sublevels leads to $\eta_+ = \eta_-$ and hence $\phi_{\text{th}}(\omega, t) = 0$, while $\alpha_{\text{th}}(\omega, t)$ is proportional to the number density. In an atomic population that has been optically pumped by linearly polarized light, coherences appear between the Zeeman sublevels with $\Delta m_F = 2$, which leads to $\eta_+ \neq \eta_-$ (see Appendix A). In this case, the absorption is modified and a rotation of the polarization angle of the transmitted probe is observed.

In the presence of a longitudinal magnetic field, the energies of the ground-state Zeeman sublevels are split by the Larmor frequency, $\Omega_L = m_F \mu_B g_F B / \hbar$, where m_F is the magnetic quantum number, μ_B is the Bohr magneton, g_F is the hyperfine Landé g factor, B is the magnetic field strength, and \hbar is the reduced Planck constant. If an initially polarized medium is allowed to freely relax (i.e., free-induction decay), then the coherences between states with $\Delta m_F = 2$ will evolve at a frequency of $2\Omega_L$ [27,28]. In this case, $\text{Re}[\eta_+(\omega, t) - \eta_-(\omega, t)]$ contains a component that oscillates at a frequency of $2\Omega_L$ (see Appendix A), resulting in modulation of the plane of polarization of the probe laser at the same frequency.

In order to maximize the polarization of the medium at a nonzero magnetic field, one can optically pump the medium with a laser that is amplitude modulated at a frequency $\Omega_m \sim 2\Omega_L$. In this case, the probe beam will show a modulation of the plane of polarization at the driving frequency Ω_m and will be resonantly enhanced if $\Omega_m = 2\Omega_L$ [29].

The narrow spectral width of the pump means that it can only directly optically pump atoms that reside in a relatively narrow spectral window (set by the power-broadened width of the pump-atom interaction). At first sight, one might expect that the probe will only observe a relatively narrow peaked spectrum of polarized atoms. However, in a cell with an antirelaxation coating, atoms may bounce from the wall while maintaining their ground-state coherence. This process produces a thermalization of their longitudinal velocity so that typical experiments observe polarization across the full Doppler-broadened spectrum. However, these temporally and spectrally resolved frequency-comb observations allow us to directly observe two different populations of polarized atoms contributing to the optical rotation of the probe—the atoms that have taken a direct pathway from the pump to the probe, as well as those that have bounced from the cell wall in the time between those two interactions.

These two atomic populations are distinguishable by their spectral distributions. Polarized atoms that have taken the direct pathway between pump and probe regions show a narrow spectral peak that rapidly disappears, while atoms that have bounced from the cell wall exhibit a longer-lived Gaussian-shaped spectrum:

$$\phi_{\text{th}}(\omega) = \sum_i \phi_i \exp \left[-\frac{(\omega - \omega_i)^2}{2\sigma^2} \right], \quad (6)$$

characterized by the Doppler width σ and a center frequency ω_i and where ϕ_i is the peak optical rotation of the i th transition. The sum in this case is performed over all hyperfine transitions. The probe absorption also shows a typical thermal velocity distribution because the atomic vapor is in thermal equilibrium with the cell walls:

$$\alpha_{\text{th}}(\omega) = \sum_i \alpha_i \exp \left[-\frac{(\omega - \omega_i)^2}{2\sigma^2} \right], \quad (7)$$

where α_i is the peak optical depth on the i th resonance and all other terms are defined as per Eq. (6). Our measurements show that the Doppler width of the optical rotation spectrum in Eq. (6) and the width in Eq. (7) are identical within experimental error.

The unique ability of the frequency comb to isolate the two polarized atomic populations enables us to make two independent estimates of the fraction of polarized atoms within the cell. The first approach recognizes that unpolarized atoms make no contribution to the optical rotation, while making the predominant contribution to the optical absorption. This approach gives us the opportunity to directly measure the fraction of the polarized atoms by taking the ratio of Eqs. (6) and (7). Employing the three-level density matrix model detailed in Appendix A, we can simplify the ratio of the optical rotation amplitude to the optical depth for the two ^{87}Rb hyperfine transitions spanned by the frequency comb:

$$\frac{\phi_i(\omega)}{\alpha_i(\omega)} = 0.63\epsilon, \quad (8)$$

where i corresponds to the i th hyperfine transition and $\epsilon = N_\phi/N$ is the fractional density of polarized atoms, where N_ϕ is the density of optically pumped atoms which generate optical rotation and N is the total atomic number density. The prefactor originates from averaging the ratio over a given observation time based on the experimental parameters used below.

IV. RESULTS

A. Free-induction decay

The capability of the EOFC to resolve the spectral and temporal evolution of the optical rotation is demonstrated by observing the free-induction decay of the atomic

polarization. A CW laser optically pumps the $F = 2 \rightarrow F' = 1$ hyperfine transition of the ^{87}Rb D₁ manifold to create a steady-state atomic polarization. The evolution of the decay is then observed with the EOFC after the pump light is switched off (cf. Fig. 3).

A number of strong features are evident in Fig. 3. In the time domain, the optical rotation shows an exponentially damped sinusoidal modulation. This modulation is a result of the applied approximately $0.8\text{-}\mu\text{T}$ magnetic field producing a Larmor frequency of $\Omega_L/2\pi = 5.7\text{ kHz}$. The exponential decay has a time constant of $100\text{ }\mu\text{s}$, which reflects the relatively poor quality of the antirelaxation coating in this particular cell [30–32]. Additionally, the optical rotation for the two hyperfine transitions, $F = 2 \rightarrow F' = 1, 2$, is observed to evolve out of phase due to a sign difference between their respective Clebsch-Gordan coefficients (cf. Appendix B).

The pump laser is red detuned 175 MHz from the center of the Doppler profile of the $F = 2 \rightarrow F' = 1$ transition and hence can only polarize atoms within a narrow velocity class. However, as described earlier, the line shape of the optical rotation spectrum (cf. Fig. 3(b) for detailed cross sections) is much broader than the spectral width of the pump and exhibits predominantly a Gaussian line shape, particularly for measurements greater than $20\text{ }\mu\text{s}$ after the pump beam is switched off. As described earlier, the Gaussian line shape arises due to the atomic velocities of the polarized atoms that have been thermalized by one or more wall collisions prior to entering the probe region [33]. This is in line with previous experiments, which show that only a small number of collisions with the cell walls is sufficient to reproduce the full Doppler profile for a gas [34].

A closer examination of the initial time steps in Fig. 3(b) reveals a peaked structure that differs from the Gaussian line shape but decays within approximately $20\text{ }\mu\text{s}$. We postulate that this anomaly is associated with a small number of atoms that are optically polarized by the pump and then travel directly into the probe beam without interacting with the cell walls [35]. The timescale for the rapid decay is consistent with the typical time for an atom to transit from the pump to the probe beam ($\tau_{\text{tr}} \sim 33 \pm 14\text{ }\mu\text{s}$, where the errors are from the uncertainty in the pump and probe separation). To analyze this feature in more detail, we generate a significantly enhanced atomic polarization using a synchronous-optical-pumping technique.

B. Synchronously pumped optical rotation

The synchronous-optical-pumping technique achieves a large steady-state atomic polarization by modulating the pump amplitude at the second harmonic of the Larmor frequency, $\Omega_m = 2\Omega_L$. In this experiment, we generate a 100% amplitude modulation of the pump with a 25% duty cycle at a rate of $\Omega_m/2\pi = 10\text{ kHz}$. The atomic

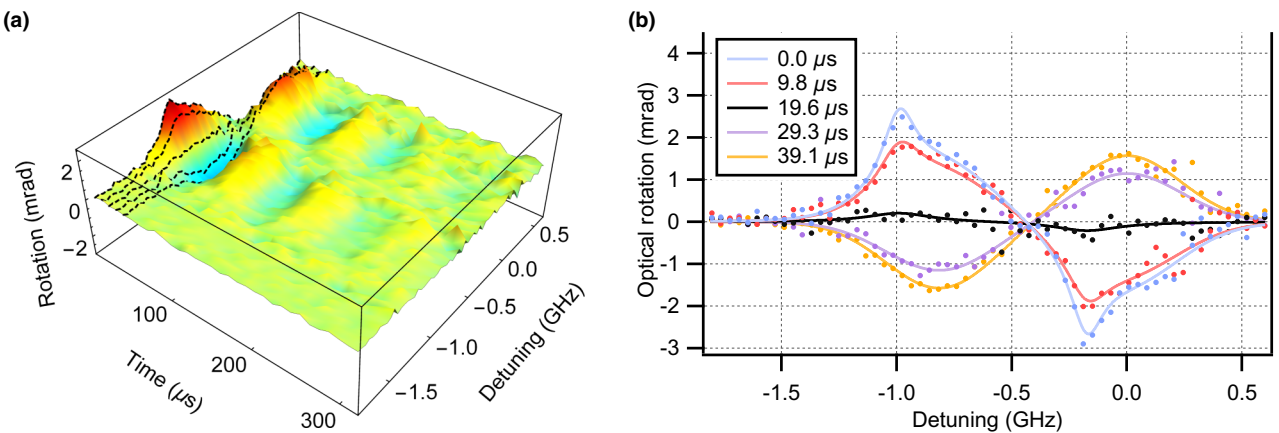


FIG. 3. (a) Three-dimensional surface plot of the optical rotation of the electro-optic frequency comb using the free-induction decay technique for the $^{87}\text{Rb } F = 2 \rightarrow F' = 1, 2$ transitions at a relative detuning of -0.82 and 0.0 GHz, respectively. The temporal and spectral resolutions are $\Delta t = 9.78 \mu\text{s}$ and $\Delta\nu = 39.37 \text{ MHz}$, respectively. The data are averaged 400 times, with the atomic-linear-polarization response removed in postprocessing. (b) Spectra for the first five time steps indicated by the dashed lines on the surface plot. Each spectrum is fit using Eq. (10), where the fitting parameters have been held fixed using those obtained from fitting Eq. (3) to Fig. 2.

response in the temporal and spectral domains (cf. Fig. 4) exhibits similar features to the FID data; however, the synchronous optical pumping allows us to average over multiple pumping cycles.

The time-domain optical rotation $\phi_{\text{exp}}(t)$ for the central comb modes of the two hyperfine transitions is displayed in Fig. 4(b). A relatively nonsinusoidal optical rotation is observed in these data due to a combination of inadvertently detuning from the resonance condition ($\Omega_m = 2\Omega_L$) by one resonance width (approximately 1.5 kHz) and ground-state relaxation between pumping pulses. As a result, each comb mode's optical rotation is only fitted during the period in which the pump beam is switched off. In this case, the optical rotation signals exhibit the following form:

$$\phi_{\text{fit}}(t) = a \sin(\omega t + \varphi) \exp\left(-\frac{t}{\tau}\right) + c, \quad (9)$$

where ω is the angular frequency; a is the optical rotation amplitude; φ is the phase; τ is the spin-relaxation time,

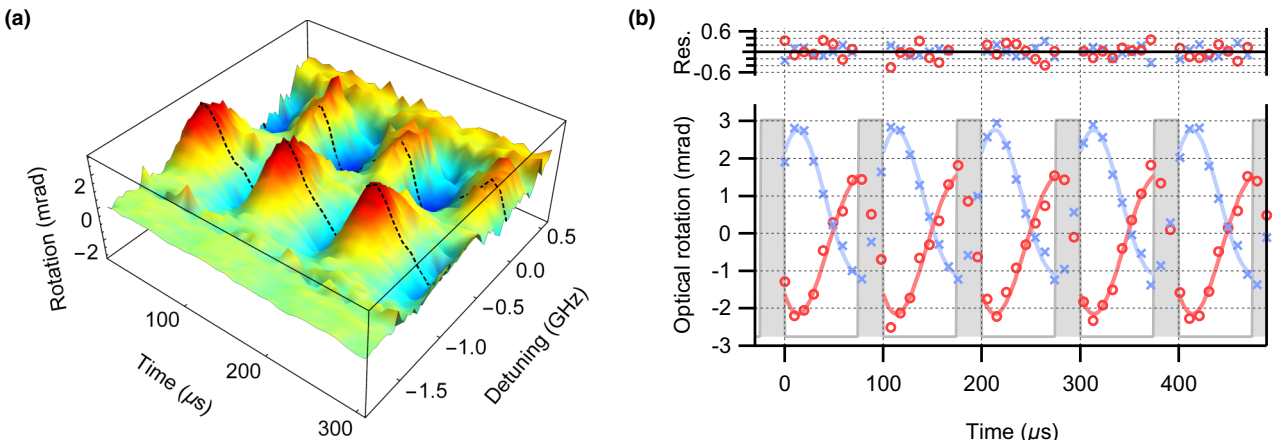


FIG. 4. (a) Three-dimensional surface plot of the optical rotation of the electro-optic frequency comb using the synchronous-optical-pumping technique for the $^{87}\text{Rb } F = 2 \rightarrow F' = 1, 2$ transitions at a relative detuning of -0.86 and 0.0 GHz, respectively. Dashed lines indicate the central comb mode for each hyperfine transition. The temporal and spectral resolutions are $\Delta t = 9.78 \mu\text{s}$ and $\Delta\nu = 39.37 \text{ MHz}$, respectively. The data are averaged 400 times with the atomic-linear-polarization response removed in postprocessing. (b) Optical rotation measured by the center comb modes of the hyperfine transitions (dashed lines on the surface plot) when pumped at a modulation frequency of $\Omega_m \sim 2\Omega_L$. Blue markers (crosses) correspond to the $F = 2 \rightarrow F' = 1$ hyperfine transition, while the red markers (circles) correspond to the $F = 2 \rightarrow F' = 2$ transition. A sinusoidal fitting function, Eq. (9), is applied to the comb data, with the pump-beam modulation shaded in gray.

which is held fixed at $\tau = 100 \mu\text{s}$, obtained from fitting the FID data presented in Fig. 3; and c is an offset that accounts for the nonuniform optical rotation due to the optics over the span of the broadband comb.

We plot the optical rotation amplitude a for each of the comb modes in Fig. 5, which shows an improved signal-to-noise ratio when compared to the FID data presented in Fig. 3(b). The optical rotation spectrum $\phi(\omega)$ is modeled as

$$\phi_{\text{fit}}(\omega) = \sum_i \mathcal{L}_i(\omega - \omega_i - \omega_p) + \mathcal{G}_i(\omega - \omega_i), \quad (10)$$

where ω is angular frequency; ω_i is detuning relative to the $F = 2 \rightarrow F' = 2$ transition; ω_p is the pump detuning from resonance; and the sum is performed over the $F = 2 \rightarrow F' = 1, 2$ hyperfine transitions. As described in Sec. III, atoms that travel directly from the pump to the probe region should reflect the velocity-selective nature of the atom-light interaction and should therefore give rise to a Lorentzian spectral signature, $\mathcal{L}_i(\omega - \omega_i - \omega_p)$. A second group of atoms enters the probe region following one or more wall collisions and produces a Gaussian spectral profile $\mathcal{G}_i(\omega - \omega_i)$ due to the thermalization of the atoms' velocity along the probe-beam propagation vector.

The optical rotation spectrum presented in Fig. 5 has been fit using Eq. (10), with the Doppler width fixed at the value extracted from the transmission spectrum (cf. Fig. 2). Only three free parameters are allowed in the fitting algorithm: the amplitude of the two Gaussian components

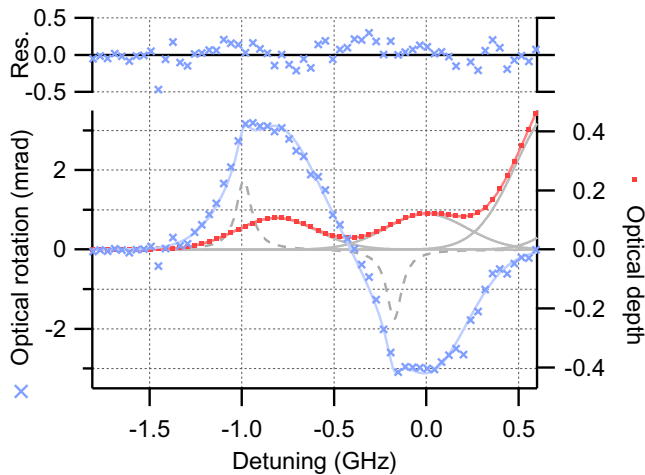


FIG. 5. Spectral dependence of the optical rotation amplitude a (blue markers) and average optical depth of the two polarization components (red dots) of each comb mode. The red line is a fit to the red dots using Eq. (3), while the blue line is a fit to the blue markers using Eq. (10). Also presented are the spectral contributions to the optical depth from each hyperfine transition (gray lines), along with Lorentzian contributions to the optical rotation amplitude (dashed gray line) that have been scaled by a factor of 2 for visibility. Two ^{85}Rb hyperfine transitions ($F = 3 \rightarrow F' = 2, 3$) extend off the graph at positive detuning.

and the amplitude and width of the two Lorentzian features (which are assumed to be the same for the two resonances). The Lorentzian detuning ω_p is found to be consistent with the known pump frequency, while the fitted width of approximately 100 MHz is consistent with the power broadening expected from a pump beam with an input intensity that is around 200 times above the saturation intensity.

The extracted amplitude of the Gaussian component of the rotation spectrum in Fig. 5 is $\phi = 3.06 \text{ mrad}$, while the optical depth in Fig. 2 is $\alpha = 0.11$. As outlined in Sec. III, these two values, along with Eq. (8), can be used to estimate that the fraction of polarized atoms within the vapor is approximately 4.4%. An approximate estimate of the expected number of polarized atoms can be derived from the knowledge that the pump can only interact with about 20% of the atoms in the thermal distribution (as shown in Fig. 5), that the pump has an effective pumping volume of around 36% of the cell (2-cm diameter) in a single pump interaction of $25 \mu\text{s}$ duration with a typical thermal velocity of rubidium (245 ms^{-1} at 42°C), and that the spin-relaxation time is approximately $100 \mu\text{s}$. This combination of effects leads to an expected polarized population averaged over the pump cycle of around 5%, which is in good agreement with the experimental observation.

The comb also allows an estimate of the quality of the antirelaxation coating by considering the relative fraction of optically polarized atoms that enter the probe via the two possible routes: either directly from the pump to the probe regions or through one or more wall collisions. The amplitude of the Lorentzian component shown in Fig. 5 is about 30% of the Gaussian component, which indicates the relative density of atoms arriving via the two pathways. On the other hand, Monte Carlo modeling using the size of the two beams (1.5- and 3.5-mm $1/e^2$ diameter) and their separation (6–10 mm) suggests that only about 3%–9% of the atoms leaving the pump beam should directly pass through the probe region. This result suggests that about 75% of atoms bouncing from the cell wall maintain their ground-state coherence, which is consistent with the spin-relaxation time of this cell (approximately $100 \mu\text{s}$, corresponding to a few bounces before relaxation).

C. Noise comparison between EOFC and CW probing

A key determination is whether the additional information that is extracted by the EOFC comes at the cost of a noise penalty. For these purposes, we made a careful comparison to a conventional single-frequency probe beam on the same experiment.

A total comb power of $500 \mu\text{W}$ is incident on the vapor cell, which corresponded to around $4 \mu\text{W}$ of optical power per mode for modes near the center of the comb. The cell transmission, polarization splitting at the Wollaston prism, and coupling to the photodetectors reduces the detected

power per mode to around $0.3 \mu\text{W}$. The signals from each comb mode are detected using a heterodyne read-out with a local oscillator of much higher power, in which case the shot noise of each comb mode is the dominant noise source [36]. The calculated shot-noise-limited sensitivity for a single comb mode is approximately $26 \mu\text{rad}$ (cf. Appendix C). The fit residuals presented in Fig. 4(b) have a standard deviation of approximately $150 \mu\text{rad}$, around a factor of 6 above the shot-noise limit. The current performance limit is set by electronic noise of the photodetectors as confirmed by a dark-current measurement.

We compare the EOFC measurements with a CW probe measurement. In this case, the magnetic field and corresponding pump modulation frequency are $2.9 \mu\text{T}$ and $\Omega_m/2\pi = 40 \text{ kHz}$, respectively. The probe beam had an optical power of $100 \mu\text{W}$ and is tuned to the center of the $F = 2 \rightarrow F' = 1$ hyperfine transition of the $^{87}\text{Rb D}_1$ manifold. The optical rotation signal measured by this probe beam is presented in Fig. 6, along with a fit using Eq. (9). The fit residuals have a standard deviation of $3 \mu\text{rad}$. Using a similar approach to that detailed in Appendix C, the shot-noise-limited optical rotation is readily calculated from the power on the photodetector along with Eq. (2) to be $0.5 \mu\text{rad}$ in the measurement bandwidth. This measurement is therefore a factor of 6 from the shot-noise limit and is consistent with the electronic noise of the photodetectors.

In the particular conditions here, photodetector noise set the limit because we chose to use relatively low probe powers to minimize the perturbation of the ground-state

atomic coherence. A change in experimental conditions is likely to yield shot-noise-limited EOFC measurements. The perhaps surprising observation here is that there is no significant introduction of noise arising from the use of a comb-based probe despite the additional information that is acquired from the atomic system.

V. CONCLUSION

We demonstrate the ability of an electro-optic frequency comb to simultaneously observe the Larmor precession of rubidium atoms in the temporal and spectral domains. The free-induction decay of the atomic vapor is observed on both the $F = 2 \rightarrow F' = 1, 2$ transitions, which shows the optical rotation of the two manifolds oscillating out of phase due to sign differences of the Clebsch-Gordan coefficients between the two transitions. We also observe the exponential decay of the atomic polarization due to collisions with the cell walls. The comb observations allow us to distinguish two groups of polarized atoms: those that have undergone one or more wall collisions, which exhibit a Doppler-broadened spectral profile, and those that have followed a direct path between the pump and probe regions, which show a much narrower spectral feature that rapidly relaxes.

We compare the rotational sensitivity performance of the comb measurement with that of a continuous-wave measurement and show that both techniques can approach the shot-noise limit. The comb technique thus allows rapid temporally and spectrally resolved measurements to be performed without introducing a significant amount of noise with respect to a continuous-wave measurement.

ACKNOWLEDGMENTS

The authors acknowledge financial support from Scott Foster at the Defence Science and Technology Group together with support from the South Australian Government through the Premier's Science and Research Fund. The authors also wish to acknowledge financial support from the National Science Centre within the Opus Program.

APPENDIX A: DENSITY MATRIX THEORY

The dynamics of the ^{87}Rb atoms in the pump and probe beams are independent as there is no cross-sectional overlap between the two beams. The interaction between the pump and probe is therefore mediated by atoms traversing these two beams. In order to model the observed optical rotation signals, it is necessary to incorporate both the pumping and probing processes, as well as the kinetics that lead to atoms traversing through two separate optical fields.

The ^{87}Rb atoms are initially optically pumped by the pump beam, which is tuned to the $F = 2 \rightarrow F' = 1$

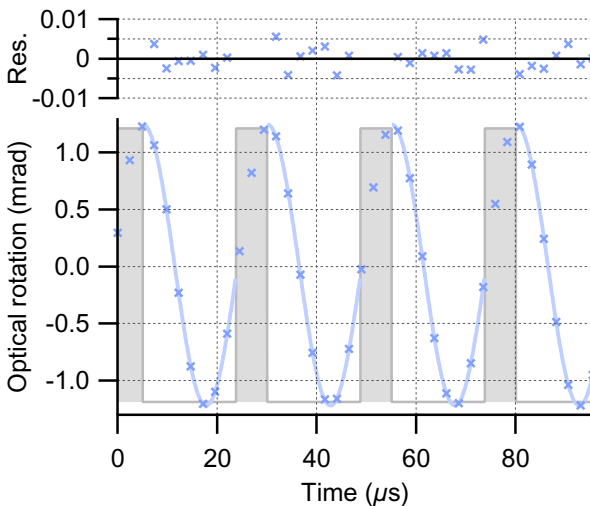


FIG. 6. Optical rotation measurements using a conventional CW laser tuned to the center of the $F = 2 \rightarrow F' = 1$ hyperfine transition of the $^{87}\text{Rb D}_1$ manifold. The data presented (blue markers) are averaged 2048 times and fitted (blue line) using Eq. (9). The pump-beam modulation is shaded in gray. An offset due to misbalancing the polarimeter has been removed in postprocessing.

hyperfine transition with a Rabi frequency of $\Omega \approx 56$ MHz—much larger than the decay rate of the excited state, $\Gamma = 5.75$ MHz. A strongly driven optical transition such as this, $\Omega \gg \Gamma$, results in the $F = 2$ ground state being rapidly optically pumped into a population distribution, which forms a dark state, established on a timescale of Γ^{-1} . This dark state exhibits negligible absorption and thus slows the optical pumping of atoms into the uncoupled $F = 1$ ground state. Since the atomic population is “trapped” in the $F = 2$ ground state during the pumping process, with little population dynamics, this enables the system to be simplified into a three-level model to better understand the pumping and probing processes.

The simplified energy-level diagram used in these calculations is shown as red arrows in the inset of Fig. 2. The quantization axis is defined to be in the direction of the magnetic field, which is parallel to the pump and probe beams. The linearly polarized pump and probe beams can be decomposed into two circularly polarized components, leading to our simple model using only three energy levels: two ground states $|m_1\rangle$ and $|m_{-1}\rangle$ and a single excited state $|e\rangle$. The excited-state decay rate is given by Γ , while the relaxation of the ground states due to dephasing collisions is given by γ . A first-order approximation to the full model of the ^{87}Rb atoms can be reproduced by summing a number of these simplified models together that cover all of the ground and excited states.

The temporal evolution of the density matrix ρ , representing the simple model in both beams, is governed by the Liouville equations [37]. The Liouville equations governing the dynamics of the simple model atom take the general form

$$\frac{d\rho}{dt} = -\frac{i}{\hbar} [\mathcal{H}_{\text{atom}} + \mathcal{H}_{\text{int}}, \rho] + \Lambda(\rho), \quad (\text{A1})$$

where the atomic and light-atom interaction Hamiltonians under the rotating wave approximation are given by

$$\mathcal{H}_{\text{atom}} + \mathcal{H}_{\text{int}} = \hbar \begin{pmatrix} \Omega_L & 0 & \Omega/2 \\ 0 & -\Omega_L & -\Omega/2 \\ \Omega/2 & -\Omega/2 & -\Delta \end{pmatrix}, \quad (\text{A2})$$

where Ω_L is the Zeeman splitting of the ground states relative to the $|m_0\rangle$ ground state, Δ is the optical detuning of the laser field from the atomic transition frequency, and Ω is the Rabi frequency of the atom-light interaction given by

$$\Omega = \frac{\mu E_0}{\hbar}, \quad (\text{A3})$$

where E_0 is the amplitude of the driving electric field and μ is the electric dipole moment for the $|m_{\pm 1}\rangle \rightarrow |e\rangle$ transition.

Relaxation is included via the Λ term which takes the form

$$\Lambda(\rho) = \frac{\Gamma}{2} \begin{pmatrix} \rho_{e,e} & 0 & -\rho_{m_1,e} \\ 0 & \rho_{e,e} & -\rho_{m_{-1},e} \\ -\rho_{e,m_1} & -\rho_{e,m_{-1}} & -2\rho_{e,e} \end{pmatrix} + \frac{\gamma}{2} \begin{pmatrix} 1 & 0 & 0 \\ 0 & 1 & 0 \\ 0 & 0 & 0 \end{pmatrix} - \gamma\rho. \quad (\text{A4})$$

The first line is the contribution from spontaneous decay, while the second line contains the contributions from ground-state repopulation and relaxation, respectively.

The atomic system approaches a steady state on a timescale of Γ^{-1} , which is much shorter than both the time taken for the atoms to cross the pump beam and the time in which the pump beam is switched on. As a result, the simplified atomic system leaves the pump beam having been optically pumped to a steady state, with a population distribution and coherences given by

$$\rho_{m_1,m_1} = \rho_{m_{-1},m_{-1}} = 1/2, \quad (\text{A5})$$

$$\rho_{m_1,m_{-1}} = \rho_{m_{-1},m_1} = -1/2, \quad (\text{A6})$$

with all other terms equal to zero when $\Omega_{m\pm 1,e} \gg \Omega_L, \Gamma, \gamma$. After the pump light is switched off, the atomic system undergoes free evolution, which results in an oscillatory response of the ground-state coherences given by

$$\rho_{m_1,m_{-1}} = \rho_{m_{-1},m_1}^* = \frac{1}{2} e^{-\gamma t} e^{i2\Omega_L t}. \quad (\text{A7})$$

It can be seen that the coherences evolve at a frequency of $2\Omega_L$, which is the frequency separation between the two ground-state Zeeman sublevels, $|m_1\rangle$ and $|m_{-1}\rangle$, and decay at a rate of γ due to ground-state relaxation.

The atomic interaction with the probe beam can be greatly simplified under the assumption that the probe does not significantly perturb the atomic populations. This is a valid assumption given the relatively low optical power of the probe beam. When the steady-state populations and the freely evolving ground state coherences are substituted into Eq. (A1), the resulting time-dependent coherences between states $|m_{\pm 1}\rangle$ and $|e\rangle$ are given by

$$\frac{d\rho_{m_{\pm 1},e}}{dt} = \pm \frac{i\Omega}{4} (1 - e^{-\gamma t} e^{\mp 2it\Omega_L}) - \left[\gamma + \frac{\Gamma}{2} + i(\Delta \pm \Omega_L) \right] \rho_{m_{\pm 1},e}, \quad (\text{A8})$$

where Ω is the Rabi frequency of the probe light. Solving this equation for $t \gg \Gamma^{-1}$ yields the solution:

$$\rho_{\pm 1,e} \approx A_{\pm} + B_{\pm} e^{-\gamma t} e^{\mp i(2\Omega_L t + \theta_{\pm})}. \quad (\text{A9})$$

The first term, A , represents the dc atomic response, which is present even when the pump beam is switched off, and

corresponds to the typical two-level absorption. The second term, which oscillates at a frequency of $2\Omega_L$, is the nonlinear magneto-optical rotation. This term is induced by the pump beam generating coherence between the two ground-state Zeeman sublevels and is observed experimentally. The coefficients A_{\pm} and B_{\pm} and the phase of the coherences θ_{\pm} are given by

$$A_{\pm} = \pm \frac{\Omega_{m_{\pm 1},e}}{2} \frac{i(\Gamma + 2\gamma) + 2(\Delta \pm \Omega_L)}{(\Gamma + 2\gamma)^2 + 4(\Delta \pm \Omega_L)^2}, \quad (\text{A10})$$

$$B_{\pm} = \frac{\Omega_{m_{\pm 1},e}}{2} \frac{1}{\sqrt{\Gamma^2 + 4(\Delta \mp \Omega_L)^2}}, \quad (\text{A11})$$

$$\theta_{\pm} = \arctan [\mp 2(\Delta \mp \Omega_L), \Gamma], \quad (\text{A12})$$

The optical depth and optical rotation for an optically thin media can be calculated from [37]

$$\alpha = \frac{N\omega\hbar l}{\sqrt{2}} \frac{\Omega}{I} \operatorname{Im}(\rho_{m_{-1},e} - \rho_{m_1,e}), \quad (\text{A13})$$

$$\phi = -\frac{N\omega\hbar l}{\sqrt{2}} \frac{\Omega}{I} \operatorname{Re}(\rho_{m_{-1},e} + \rho_{m_1,e}), \quad (\text{A14})$$

where N_{ϕ} is the density of optically pumped atoms that generate optical rotation; N is the total atomic number density; l is the optical path length through the ^{87}Rb vapor; and I is the optical intensity, which is given by

$$I = \frac{c\epsilon_0|E_0|^2}{2}, \quad (\text{A15})$$

where ϵ_0 is the vacuum permittivity and c is the speed of light. Taking the ratio of the oscillating optical rotation to the steady-state optical depth when on resonance (i.e., $\Delta = 0$) using the solution to the density matrix, Eq. (A9), and noting that $\Omega_L \ll \Gamma$ leads to

$$\begin{aligned} \frac{\phi}{\alpha} &= \frac{N_{\phi}}{N} \frac{\operatorname{Re}(\rho_{m_{-1},e} + \rho_{m_1,e})}{\operatorname{Im}(\rho_{m_{-1},e} - \rho_{m_1,e})}, \\ &= \frac{N_{\phi}}{N} \frac{\operatorname{Re}(B_- + B_+)}{\operatorname{Im}(A_- - A_+)}, \\ &= \frac{N_{\phi}}{N} \frac{(2\gamma + \Gamma)^2 + 4\Omega_L^2}{(2\gamma + \Gamma)\sqrt{\Gamma^2 + 4\Omega_L^2}} e^{-\gamma t}, \\ &\approx \frac{N_{\phi}}{N} e^{-\gamma t}. \end{aligned} \quad (\text{A16})$$

The second line follows from the fact that we are considering the amplitude of the oscillating optical rotation

at the resonant frequency, $2\Omega_L$, while the measured optical depth is the dc component. The final line follows from the excited-state decay rate being much faster than both the Larmor frequency and the ground-state relaxation rate, i.e., $\Gamma \gg \Omega_L, \gamma$. As the optical rotation $\phi(t)$ decays due to ground-state relaxation, the ratio between the optical rotation and optical depth also exponentially decays with time.

Atoms that contribute to the optical rotation signal are those that possess coherence between the ground-state Zeeman sublevels upon being probed. On the other hand, all available atoms contribute to the optical depth measured by the probe beam. Thus, the relative density of polarized atoms, $\epsilon = N_{\phi}/N$, can be directly related to the ratio of the optical rotation to the optical depth using Eq. (A16). For the experimental parameters used here, i.e., a ground-state relaxation rate of $\gamma \approx 10^4$ Hz and a pumping period of $t_0 = 100 \mu\text{s}$, the fraction of polarized atoms is given by

$$\begin{aligned} \frac{\phi}{\alpha} &= \frac{1}{t_0} \int_0^{t_0} \frac{N_{\phi}}{N} e^{-\gamma t} dt, \\ &= 0.63\epsilon, \end{aligned} \quad (\text{A17})$$

which is in good agreement with experimental observations. The validity of this simplified model is checked against a numerical model that incorporated the full ^{87}Rb energy-level structure, with both models predicting a similar result to Eq. (A17).

APPENDIX B: HYPERFINE PHASE SHIFT

The π phase shift between the two hyperfine transitions observed in Fig. 4 is the result of a sign difference of the Clebsch-Gordan coefficients between right- and left-circularly polarized light for the two transitions. This can clearly be seen when evaluating the simplified model shown in Fig. 2. In order to model the $F = 2 \rightarrow F' = 1$ hyperfine transition of the ^{87}Rb D₁ manifold, two of the five ground states, $|m_{\pm}\rangle = |F = 1, m_f = \pm 1\rangle$, and one of the three excited states, $|e\rangle = |F' = 1, m_f = 0\rangle$, are considered (cf. Appendix A). After implementing the rotating-wave approximation, the light-atom interaction Hamiltonian for this transition is given by

$$\mathcal{H}_{2,1} = \frac{\hbar\Omega_{2,1}}{2} \begin{pmatrix} 0 & 0 & 1 \\ 0 & 0 & 1 \\ -1 & -1 & 0 \end{pmatrix}, \quad (\text{B1})$$

where $\Omega_{2,1}$ is the Rabi frequency for the $F = 2 \rightarrow F' = 1$ transition. However, using the same approximations, the interaction Hamiltonian for the $F = 2 \rightarrow F' = 2$ hyperfine

transition exhibits a sign change of two of the elements:

$$\mathcal{H}_{2,2} = \frac{\hbar\Omega_{2,2}}{2} \begin{pmatrix} 0 & 0 & 1 \\ 0 & 0 & -1 \\ -1 & 1 & 0 \end{pmatrix}. \quad (\text{B2})$$

The elements in question correspond to one of the circular components of the linearly polarized light. Changing the sign of these elements produces a π phase shift between the observed optical rotation in the two hyperfine transitions.

APPENDIX C: SHOT-NOISE CALCULATION FOR THE EOFC

Provided that the power of the local oscillator (LO) is significantly greater than the comb power (as is the case here), the effective shot noise for each mode is independent of the LO and is instead proportional to the power in the mode [36,38]. To calculate the resulting shot-noise-limited rotation noise, we substitute the shot noise of each of the photodetectors into Eq. (2):

$$\sigma_\phi = \sqrt{\left(\frac{\partial\phi}{\partial P_1}\sigma_{P_1}\right)^2 + \left(\frac{\partial\phi}{\partial P_2}\sigma_{P_2}\right)^2}, \quad (\text{C1})$$

where P_1 and P_2 are the optical powers measured at the two photodetectors, σ_{P_1} and σ_{P_2} are the shot-noise-induced power fluctuations of the two photodetectors, and σ_ϕ is the optical rotation noise. For a balanced polarimeter, the optical power on each photodetector is approximately equal ($P_1 \approx P_2$) and hence so is the shot noise $\sigma_{P_1} \approx \sigma_{P_2}$. This simplifies Eq. (C1) to

$$\sigma_\phi = \sqrt{2} \frac{\partial\phi}{\partial P_1} \sigma_{P_1}. \quad (\text{C2})$$

Calculation of the partial derivative and subsequent simplification yields

$$\sigma_\phi = \frac{1}{2\sqrt{2}} \frac{\sigma_{P_1}}{P_1}. \quad (\text{C3})$$

Since the optical power on the photodetector is linearly proportional to the photocurrent I , Eq. (C3) can be rewritten in terms of current as

$$\sigma_\phi = \frac{1}{2\sqrt{2}} \frac{\sigma_{I_1}}{I_1}, \quad (\text{C4})$$

where I_1 is the photocurrent of one of the photodetectors and σ_{I_1} is the root-mean-square current due to shot noise.

The current shot noise can be calculated from

$$\sigma_I = \sqrt{\frac{2eI}{\Delta t N}}, \quad (\text{C5})$$

where e is the charge of an electron, I is the photocurrent, Δt is the measurement time, and N is the number

of averages. For a detected power per mode of around $0.3 \mu\text{W}$, we calculate that the photocurrent produced by the photodetector (responsivity of 0.1 A/W at 795 nm) is $I_1 = 0.03 \mu\text{A}$. The total measurement time for a single comb mode shown in Fig. 4 is 400 averages of a $9.78-\mu\text{s}$ measurement, yielding an estimated rotational shot noise of $20 \mu\text{rad}$. In addition, we use a calibration spectrum that increases this noise by a factor of $\sqrt{2}$, giving rise to a root-mean-square rotation of $\sigma_\phi = 26.1 \mu\text{rad}$ on each comb mode.

-
- [1] G. Bison, N. Castagna, A. Hofer, P. Knowles, J.-L. Schenker, M. Kasprzak, H. Sudan, and A. Weis, A room temperature 19-channel magnetic field mapping device for cardiac signals, *Appl. Phys. Lett.* **95**, 173701 (2009).
 - [2] Svenja Knappe, Tilmann H. Sander, Olaf Kosch, Frank Wiekhorst, John Kitching, and Lutz Trahms, Cross-validation of microfabricated atomic magnetometers with superconducting quantum interference devices for biomagnetic applications, *Appl. Phys. Lett.* **97**, 133703 (2010).
 - [3] Cort Johnson, Peter D. D. Schwindt, and Michael Weisend, Magnetoencephalography with a two-color pump-probe, fiber-coupled atomic magnetometer, *Appl. Phys. Lett.* **97**, 243703 (2010).
 - [4] Shoujun Xu, Valeriy V. Yashchuk, Marcus H. Donaldson, Simon M. Rochester, Dmitry Budker, and Alexander Pines, Magnetic resonance imaging with an optical atomic magnetometer, *Proc. Natl. Acad. Sci. U.S.A.* **103**, 12668 (2006).
 - [5] G. Bison, R. Wynands, and A. Weis, A laser-pumped magnetometer for the mapping of human biomagnetic fields, *Appl. Phys. B* **76**, 325 (2003).
 - [6] H. B. Dang, A. C. Maloof, and M. V. Romalis, Ultrahigh sensitivity magnetic field and magnetization measurements with an atomic magnetometer, *Appl. Phys. Lett.* **97**, 151110 (2010).
 - [7] M. Smiciklas, J. M. Brown, L. W. Cheuk, S. J. Smullin, and M. V. Romalis, New Test of Local Lorentz Invariance using a $^{21}\text{Ne}-\text{Rb}-\text{K}$ Comagnetometer, *Phys. Rev. Lett.* **107**, 171604 (2011).
 - [8] C. J. Berglund, L. R. Hunter, D. Krause Jr., E. O. Prigge, M. S. Ronfeldt, and S. K. Lamoreaux, New Limits on Local Lorentz Invariance from Hg and Cs Magnetometers, *Phys. Rev. Lett.* **75**, 1879 (1995).
 - [9] Szymon Pustelnik *et al.*, The global network of optical magnetometers for exotic physics (GNOME): A novel scheme to search for physics beyond the standard model, *Ann. Phys.* **525**, 659 (2013).
 - [10] Derek F. Jackson Kimball, Ian Lacey, Julian Valdez, Jerlyn Swiatlowski, Cesar Rios, Rodrigo Peregrina-Ramirez, Caitlin Montcrieffe, Jackie Kremer, Jordan Dudley, and C. Sanchez, A dual-isotope rubidium comagnetometer to search for anomalous long-range spin-mass (spin-gravity) couplings of the proton, *Ann. Phys.* **525**, 514 (2013).
 - [11] Marcis Auzinsh and Ruvin Ferber, *Optical Polarization of Molecules* (Cambridge University Press, New York, 2005), Vol. 4.

- [12] Dmitry Budker, Valeriy Yashchuk, and Max Zolotorev, Nonlinear Magneto-optic Effects with Ultranarrow Widths, *Phys. Rev. Lett.* **81**, 5788 (1998).
- [13] Dmitry Budker and Derek F. Jackson Kimball, *Optical Magnetometry* (Cambridge University Press, New York, 2013).
- [14] David A. Long, Adam J. Fleisher, David F. Plusquellic, and Joseph T. Hodges, Multiplexed sub-Doppler spectroscopy with an optical frequency comb, *Phys. Rev. A* **94**, 061801 (2016).
- [15] Vincente Duran, Santiago Tainta, and Victor Torres-Company, Ultrafast electrooptic dual-comb interferometry, *Opt. Express* **23**, 30557 (2015).
- [16] Nicolas Bourbeau Hébert, Vincent Michaud-Belleau, James D. Anstie, Jean-Daniel Deschênes, Andre N. Luiten, and Jérôme Genest, Self-heterodyne interference spectroscopy using a comb generated by pseudo-random modulation, *Opt. Express* **23**, 27806 (2015).
- [17] Nicolas Bourbeau Hébert, Vincent Michaud-Belleau, Christopher Perrella, Gar-Wing Truong, James D. Anstie, Thomas M. Stace, Jérôme Genest, and Andre N. Luiten, Real-time Dynamic Atomic Spectroscopy using Electro-optic Frequency Combs, *Phys. Rev. Applied* **6**, 044012 (2016).
- [18] David A. Long, Adam J. Fleisher, Kevin O. Douglass, Stephen E. Maxwell, K. Bielska, Joseph T. Hodges, and David F. Plusquellic, Multiheterodyne spectroscopy with optical frequency combs generated from a continuous-wave laser, *Opt. Lett.* **39**, 2688 (2014).
- [19] Yuan Bao, Xingwen Yi, Zhaojun Li, Qingming Chen, Jianping Li, Xudong Fan, and Xuming Zhang, A digitally generated ultrafine optical frequency comb for spectral measurements with 0.01-pm resolution and 0.7- μ s response time, *Light Sci. Appl.* **4**, e300 (2015).
- [20] Guy Millot, Stéphane Pitois, Ming Yan, Tatevik Hovhannisyan, Abdelkrim Bendahmane, Theodor W. Hänsch, and Nathalie Picqué, Frequency-agile dual-comb spectroscopy, *Nat. Photonics* **10**, 27 (2016).
- [21] Pedro Martín-Mateos, Borja Jerez, and Pablo Acedo, Dual electro-optic optical frequency combs for multiheterodyne molecular dispersion spectroscopy, *Opt. Express* **23**, 21149 (2015).
- [22] B. Patton, O. Neitzke, S. Rochester, E. Bahr, S. Guttikonda, D. F. Kimball, B. Coste, I. Novikova, and D. Budker, in *APS Division of Atomic, Molecular and Optical Physics Meeting Abstracts* (2012).
- [23] Daniel Adam Steck, Rubidium 87 D Line Data, <http://steck.us/alkalidata> (revision 2.1.5, 23 October 2017).
- [24] G.-W. Truong, J. D. Anstie, E. F. May, T. M. Stace, and A. N. Luiten, Accurate lineshape spectroscopy and the Boltzmann constant, *Nat. Commun.* **6**, 8345 (2015).
- [25] Wojciech Gawlik and Szymon Pustelnik, in *High Sensitivity Magnetometers*, edited by Asaf Grosz, Michael J. Haji-Sheikh, and Subhas C. Mukhopadhyay (Springer, Switzerland, 2017), p. 425.
- [26] Gordon W. F. Drake, *Springer Handbook of Atomic, Molecular, and Optical Physics* (Springer Science & Business Media, New York, 2006).
- [27] Evgeniy B. Alexandrov, Marcis Auzinsh, Dmitry Budker, Derek F. Kimball, Simon M. Rochester, and Valeriy V. Yashchuk, Dynamic effects in nonlinear magneto-optics of atoms and molecules: Review, *J. Opt. Soc. Am. B* **22**, 7 (2005).
- [28] V. Acosta, M. P. Ledbetter, S. M. Rochester, D. Budker, D. F. Jackson Kimball, D. C. Hovde, W. Gawlik, S. Pustelnik, J. Zachorowski, and V. V. Yashchuk, Nonlinear magneto-optical rotation with frequency-modulated light in the geophysical field range, *Phys. Rev. A* **73**, 053404 (2006).
- [29] W. Gawlik and S. Pustelnik, *New Trends in Quantum Coherence and Nonlinear Optics* (Nova Publishers, New York, 2009), p. 47.
- [30] Miriam T. Graf, Derek F. Kimball, Simon M. Rochester, K. Kerner, C. Wong, D. Budker, E. B. Alexandrov, M. V. Balabas, and V. V. Yashchuk, Relaxation of atomic polarization in paraffin-coated cesium vapor cells, *Phys. Rev. A* **72**, 023401 (2005).
- [31] W. Franzen, Spin relaxation of optically aligned rubidium vapor, *Phys. Rev.* **115**, 850 (1959).
- [32] S. J. Seltzer, D. M. Rampulla, S. Rivillon-Amy, Y. J. Chabal, S. L. Bernasek, and M. V. Romalis, Testing the effect of surface coatings on alkali atom polarization lifetimes, *J. Appl. Phys.* **104**, 103116 (2008).
- [33] S. I. Kanorsky, A. Weis, and J. Skalla, A wall-collision-induced Ramsey resonance, *Appl. Phys. B* **60**, S165 (1995).
- [34] C. H. Holbrow, A. P. Ghosh, D. Heinzen, X. Zhu, W. W. Quivers Jr, G. Shimkaveg, P. G. Pappas, J. E. Thomas, and M. S. Feld, Complete doppler coverage in laser optical pumping by wall-induced velocity-changing collisions, *Phys. Rev. A* **34**, 2477 (1986).
- [35] D. Budker, D. F. Kimball, S. M. Rochester, and V. V. Yashchuk, Nonlinear electro- and magneto-optical effects related to Bennett structures, *Phys. Rev. A* **65**, 033401 (2002).
- [36] J. Reichert, R. Holzwarth, T. Udem, and T. W. Hänsch, Measuring the frequency of light with mode-locked lasers, *Opt. Commun.* **172**, 59 (1999).
- [37] Marcis Auzinsh, Dmitry Budker, and Simon M. Rochester, *Optically Polarized Atoms* (Oxford University Press, New York, 2010).
- [38] Hugo Bergeron, Jean-Daniel Deschênes, and Jérôme Genest, Improving the signal-to-noise ratio of the beat note between a frequency comb and a tunable laser using a dynamically tracking optical filter, *Opt. Lett.* **41**, 4253 (2016).